On fault vs. off-fault seismicity: the role of rock vs. fault rheology

Cristiano Collettini (cristiano.collettini@uniroma1.it)
Sapienza Università di Roma https://orcid.org/0000-0002-4828-2516
Nicola De Paola
Durham University https://orcid.org/0000-0002-6367-9597
Massimiliano Barchi
Università di Perugia
Fabio Trippetta
Università di Roma La Sapienza
Elisa Tinti
Università di Roma La Sapienza

Article

Keywords:

Posted Date: March 15th, 2022

DOI: https://doi.org/10.21203/rs.3.rs-1433840/v1

Version of Record: A version of this preprint was published at Nature Communications on September 26th, 2022. See the published version at https://doi.org/10.1038/s41467-022-33373-y.

Abstract

Analysis of seismicity can illuminate active fault zone structures but also pervasive deformation occurring within large volumes of the seismogenic zone. Here we show that, for the M_w 6.5 2016–2017 Central Italy seismic sequence, seismicity not only localizes along SW-dipping normal faults, but also occurs within larger volumes of Triassic Evaporites, TE, composed of alternated anhydrites and dolostones. This off-fault and diffuse microseismicity shows a different frequency-magnitude distribution than on-fault seismicity along the structures hosting the largest events. We interpret that, during the sequence, shear strain-rate increase promoted widespread ductile deformation within TE that light-up with diffuse microseismicity. This interpretation is supported by field and laboratory observations showing that TE background ductile deformation is complex and dominated by distributed failure and folding of the anhydrites associated with boudinage fracturing and faulting of dolostones. Our results indicate that ductile crustal deformation can cause off-fault and diffuse microseismicity, which obeys to different scaling laws than on-fault seismicity on structures characterized by elasto-frictional stick-sip behaviour.

Introduction

In seismically active regions the geometry of active faults at depth is mainly determined by seismicity distribution. In the last two decades, improved techniques in earthquake location[1] and detection[2] revealed complexities of the fault zone structure that were previously obscured by location errors. For example, parallel fault strands have been documented for the San Andreas fault near Parkfield[3], orthogonal strike-slip faults were activated contemporaneously during the M7.1 Ridgecrest 2019 seismic sequence[4, 5], and both planar and listric normal faults have been imaged for the M6.3 2009 L'Aquila sequence[6]. However, during a seismic sequence, seismicity is not necessarily exclusive of the major structures activated within the seismogenic crust. In the San Jacinto fault zone, most of the low magnitude seismicity is occurring off-fault, in a zone that is several kilometres wide at seismogenic depth[7]. Ridgecrest 2019 aftershock distribution highlights a 5–10 km wide zone around the main ruptures[8]. In some fluid pressure stimulations, a broad network of distributed fractures has been activated with no evidence for alignment along a major fault[9], and in central Italy during the M6.5 2016–2017 sequence ~ 30% of diffuse seismicity has been detected[10]. To explain off-fault or diffuse seismicity several mechanisms have been proposed. These include, but are not limited to, fault step-over or fault branching[5,6], deformation accommodated by many small faults[9, 11], a wide damage zone[7, 12, 13], loading from an ongoing ductile deformation[8]. Overall, these studies emphasize that fault structure, style of deformation and rheology play a primary role in controlling the distribution of seismicity. However, to test such hypotheses would require access to constrained geological observations, and geophysical and mechanical data from a single, active region, which is rarely available. Here we integrate geological and geophysical data with laboratory experiments on the rocks composing the seismogenic layer of the Apennines to explain the large amount of off-fault seismicity observed during the M6.5 2016–2017 seismic sequence. Our results

show that such off-fault seismicity can be explained by the coexistence of brittle and ductile rheology within the Triassic Evaporites, TE, a thick sedimentary succession composed of the alternation of anhydrites and dolostones.

Results

Geology and seismicity distribution

The area struck by the 2016–2017 Central Italy seismic sequence was affected by a Late Miocene-Early Pliocene compressional phase, with about N-S trending east-verging anticlines and west-dipping thrust faults, followed by Late Pliocene–Quaternary extension with NW-SE trending normal faults (Fig. 1 and [14]). The seismic sequence started with the M_w 6.0 Amatrice earthquake on 24 August 2016 and was followed by the M_w 5.9 Visso and M_w 6.5 Norcia earthquakes on 26 and 30 October, respectively (Fig. 1a). These three mainshocks nucleated on a set of aligned SW-dipping normal faults[18-21]. The entire sequence activated an 80 km long, NW-SE trending normal fault system (Fig. 1a). The rocks composing the seismogenic layer in this portion of the Apennines are well constrained by seismic reflection profiles and deep borehole data[22,23], which have been integrated with surface geology observations, e.g., [24-27]. Near the Norcia mainshock, seismic profiles (Fig. 1) image the geometry of the subsurface structures (see details in [14]). Here the reflector corresponding to the top of the TE can be traced in the footwall of the M. Vettore fault, the structure that hosted the M_w 6.5 earthquake and produced surface breaks[15]. Below the TE, the top of the acoustic basement is located at 3.2 s Two Way Time, TWT (Fig. 1c), corresponding to 9 km of depth below sea level. The same reflector is imaged at 2.7 s TWT, corresponding to 7.5 km in the hangingwall of the Norcia Fault (Fig. 1b). Close to the Norcia hypocentre the subsurface geology can be schematically represented by carbonates and TE at depths < 4-5 km, TE at depths between 5 and 9 km and acoustic, phyllosilicate-rich basement below 9 km (Fig. 2a and details in [14]). In this area, the presence of a dense seismic network and the application of improved earthquake detection and location techniques allowed the development of comprehensive earthquake catalogues[10, 19-21]. The integration of subsurface geology with earthquake location well depicts on-fault seismicity located on the SW-dipping Vettore fault (Fig. 2 and details in [18-21]), but also highlights the presence of off-faults seismicity occurring within larger rock volumes of TE. A 6-8 km wide and up to 4 km thick zone of diffuse seismicity is located down-dip in the hangingwall of the mainshock rupture (Fig. 2a), and it mostly occurs after the Norcia mainshock (Fig. 2b vs. 2c). This seismicity extends both toward NNW and SSE along the strike of the activated Monte Vettore fault (Supplementary Fig. 1) and occurs mainly within the TE. Another example of off-fault seismicity is represented by kilometres long subvertical clusters of seismicity mostly located within the TE (C1-C3 in Fig. 2 and details in methods and Supplementary Fig. 2-4). Finally, off-fault seismicity within both TE and carbonates is also present at shallow crustal levels around major structures like the thrust fault located at about 2 km depth, in the footwall of the Vettore normal fault (Fig. 2a).

After reconstructing the geometry of the activated portions of the seismogenic layer and constraining the nature of the rocks involved in active deformation, we now analyse the frequency-magnitude distribution of on- and off-fault seismicity, respectively. We search for any systematic variation of the *b*-value, which is the seismic parameter that quantifies the proportion of small- to large-magnitude events, e.g., [28, 29]. The *b*-value is sensitive to differential stress[29, 30], fault roughness [31], and for some seismic sequences it has been used to discriminate foreshocks from aftershocks [32] but see also [33]. On-fault seismicity is constrained by selecting events within 0.5 km from the fault plane whose geometry is clearly imaged by aftershock distribution and moment tensor solution (Fig. 1 and 2). Off-fault seismicity was determined by selecting earthquakes occurring within TE in: a) the diffuse zone of seismicity located down-dip in the hangingwall of the mainshock rupture, hereinafter referred to as down-dip hangingwall seismicity, DHwS; and b) the sub vertical clusters (C1-C3 schematically reported in Fig. 2, see also Methods and Supplementary Fig. 2-4). The *b* value is calculated using the revised maximum likelihood estimate[34, 35]. Our results show that *b* values for on-fault events are different and systematically lower than those obtained for off-fault seismicity. In particular, *b*-values of on-fault and off-fault DHwS events are respectively 1.28 and 1.69 before Visso-Norcia (Fig. 3a), and respectively 1.34 and 1.51 for the entire seismic sequence (Fig. 3b, and Supplementary Table 1). Widening the on-fault at 1 km or extending the DHwS of ± 1 km along strike yields essentially the same results. The *b* value for clusters hosted in TE is in the range 1.55-1.81 (Fig. 3c, and Supplementary Table 1). We note that for the entire seismic sequence (Fig. 3b), the *b* value of DHwS is lower than that evaluated before the Visso-Norcia mainshocks. Such a reduction of *b*-value can be explained by the stress increase, e.g., [29, 30], affecting the DHwS area after the Visso-Norcia mainshocks[19]. Before the Visso-Norcia mainshocks, the DSHw is characterized by a larger *b*-value, which is comparable to those obtained for the TE clusters.

Style of deformation of Triassic Evaporites, TE

Evaporitic rocks are generally considered to act as ductile detachment horizons, even at low temperature and pressure, for many fold-and-thrust belts around the world[36], including the Apennines[22]. In some active areas, evaporitic rocks are considered relevant also for seismogenic processes[37, 38]. In the study area, the TE formation consists of a thick, mechanically complex sedimentary succession composed of centimetric- to decameter-scale interbeds of Ca-sulphate rocks, gypsum predominantly at depth < 1 km and anhydrite at greater depths[39], and dolostones. Seismic profiles and boreholes show that the average thickness of the TE succession is ~2 km, but it can increase up to 4 km due to folding and thrusting (Fig. 2a and [14]). In the seismically active area of the Apennines TE do not crop out and have been drilled only in few deep boreholes[39], whereas to the west of the active area, in western Umbria and in Tuscany, exhumed outcrops of TE are exposed[40]. TE outcrops show a complex style of deformation, across a range of scales. To describe deformation observed in the TE in both outcrops and experiments we use the following terminology. Brittle deformation refers to discrete and localized failure accommodated along fractures and faults, which display elasto-frictional behaviour and stress-drop, e.g.,[41]. Ductile deformation

refers to distributed deformation accommodated without stress drop via folding or distributed failure by pervasive cataclastic shear bands[42].

At the hundreds of meters scale, TE show ductile deformation represented by folding of the gypsum/anhydrite and boudinage of the dolostones layers (Fig. 4a and b). Folding is highlighted by gneissic transposed fabric (Fig. 4b and 4c), which derives by the superposition of tectonic fabrics on the earlier compositional layering. Folding in the anhydrite layers produces fractures and domino-like structures in the dolostone layers (Fig. 4c and c). These rotated faults in dolostones detach into gypsum/anhydrite rocks (Fig. 4d), emphasizing the interplay between brittle and ductile deformation in the rheological heterogeneous TE. Small displacement normal faults are also present at the boundary between gypsum/anhydrite rocks and dolostones (Fig. 4e). Intense fluid-assisted brittle fracturing (Fig. 4e) and small displacement normal faults are documented within the larger dolostone blocks. Large displacement (>100 m) normal faults (Fig. 5) are characterized by a fault core where most of the slip is localized along fault parallel principal slipping surfaces made of a fine-grained, dolomite-rich cataclasite[40]. The damage zone of major faults consists of foliated (fault-parallel foliation) gypsum/anhydrite rocks and heavily fractured dolostones (Fig. 5).

Rock vs. fault rheology

The rheological behaviour of dolostones and anhydrite rocks is investigated in rock deformation tests at pressure and temperature conditions equivalent to those present at seismogenic depths in the Apennines. Dolomite brittle behaviour is documented in a series of triaxial tests up to high pressure and temperature[43]. The failure mode of anhydrite samples, collected from deep boreholes in the TE of the Apennines, is shown in triaxial loading tests conducted at constant confining pressure, P_c = 100 MPa, and different levels of fluid pressure, P_f = 60, 80, 90 MPa (Fig. 6a and [44]). At low effective pressure, $P_e = P_c - P_f$, or for very high fluid pressure levels (black curves in Fig. 6a), after yielding and a phase of deformation at constant differential stress the sample undergoes brittle failure with a sudden stress-drop and the development of a localized fault and a thick, 1-2 mm, gouge layer. At higher effective pressure (blue and red curves in Fig. 6a), after yielding, the sample undergoes ductile failure at constant differential stress with no sudden stress drop and the development of a pervasive network of distributed shear bands (Fig. 6c top panel).

The integration of field observations and rock deformation tests shows that the bulk rheology of rock assemblages of TE is controlled by ductile deformation (i.e., folding and ductile failure of the anhydrites in Fig. 4, 6a). However, high pore fluid pressure conditions in the TE can also cause localized brittle failure (Fig. 6a) and the development of large displacement brittle normal faults (Fig. 5). Such faults show fault rock assemblages of cataclasites and fault gouge, which are typical of the elasto-frictional regime, e.g., [41]. Friction tests on anhydrite-dolomite fault gouges show a linear relationship between normal and shear stress, in agreement with a brittle failure envelope[45]. Anhydrite-dolomite fault gouges also show

significant fault healing and velocity weakening behaviour (Fig. 6b). This type of frictional properties indicates that TE fault cores, like those observed in the field (Fig. 5), can gain elastic strain energy when locked during the interseismic cycle, and promote frictional instabilities when, during tectonic loading, frictional strength is overcome. Frictional instabilities are frequently observed on these fault gouges (Fig. 6b and [46]). The instabilities are facilitated by grain-size reduction and localization along dolomite-rich principal slipping surfaces (Fig. 6c bottom panel), similar to those observed in the field (Fig. 5).

Discussion

The integration of geological and seismological data shows that, during the 2016–2017 Central Italy seismic sequence, seismicity occurs both on-fault, i.e., on SW-dipping normal faults[18–21] and off-fault, i.e., within larger rock volumes (Fig. 2). At depth greater than 6 km, i.e., below the mainshock nucleation, the seismicity is concentrated on 2–4 km thick, sub-horizontal (Fig. 2) and imbricated bands (Supplementary Fig. 1). Sub-horizontal aftershock geometry and extensional focal mechanisms have been used to propose that this seismicity represents an extensional detachment[18] that in some places is fragmented[21]. From the imbrication of the seismicity bands, it has been suggested reactivation of ancient thrust faults formed during the Late Miocene-Early Pliocene compressional phase, e.g., [19]. In this work, the integration of seismological, mechanical, surface and sub-surface geological data points to an alternative interpretation: the identified thick zones of microseismicity represent instead diffuse microearthquakes mainly triggered by ductile deformation of TE. In some portions of the activated volume, these thick zones of diffuse seismicity are confined at depth by thin and continuous seismicity alignments (cf. cross sections 7–9 in Supplementary Fig. 1) indicative of an extensional detachment[18, 21]. In other portions these thick zones of diffuse microseismicity are confined at depth by the top of the basement (Supplementary Fig. 1), where frictionally stable, foliated, and phyllosilicate-rich horizons favour aseismic deformation[47].

Our dataset therefore explains the observed seismicity by a bimodal deformation regime, with on-fault seismicity due to localized deformation and elasto-frictional behaviour along the major structures of the area, and off-fault seismicity due to pervasive and ductile shearing within the TE (Fig. 7). On-fault deformation is well imaged near the Norcia mainshock where earthquake distribution well-depicts the geometry of the activated SW-dipping normal fault[18–21], which can be followed with continuity from about 6 to 2 km of depth (Fig. 2). This on-fault seismicity occurs on large normal faults hosted within the carbonates and TE of the Apennines, showing fault structure and fault rocks typical of the elasto-frictional regime[40, 48–51]. Along these structures deformation is localized (Fig. 5), and fault frictional properties are prone to promote earthquake nucleation via their stick-slip behaviour (Fig. 6b).

Off-fault, diffuse seismicity occurring within large volumes of TE has been observed in a 6–8 km wide and up to 4 km thick zone, located down-dip in the hangingwall of the Norcia seismic rupture, and in kilometres long subvertical clusters at different crustal levels (Fig. 2). Here we propose that this diffuse seismicity is promoted by TE rheology (Fig. 7). Away from the major faults, TE deformation is mainly

controlled by the ductile behaviour of the anhydrites (Fig. 6a), with distributed ductile failure and folding, and associated boudinage of the dolostone rock bodies (Fig. 4). In addition, the ductile failure of the anhydrites promotes very low permeabilities[44], which favour fluid entrapment and fracturing of dolostones sealed by the anhydrites, as observed in several deep boreholes of the area[39] and during the sequence[52]. Following the mainshock, shear strain-rate increase[53, 54] and the development of fluid overpressure patches promoted brittle and ductile failure in large volumes of TE that light-up with diffuse microseismicity (Fig. 7). This microseismicity is the result of the development of fracturing and small brittle faults in the dolostones, distributed ductile failure in the anhydrites and reactivation of small displacement, gently-dipping, minor normal faults. This style of background deformation is dominated by the ductile behaviour of the TE and is associated to high *b*-values ($1.51 < b < 1.81$), indicating that these portions of the seismogenic layer are prone to activate a large number of distributed faults and fractures with limited size. On the contrary, on-fault seismicity considered for the same time-intervals shows lower b-values ($1.28 < b < 1.34$). We suggest that this different frequency-magnitude distribution for on-fault seismicity likely reflects the elasto-frictional deformation expected along the major structures of the crust characterized by stick-sip behaviour.

Our results highlight the strongly heterogeneous nature of crustal deformation, emphasizing that a significant number of micro-earthquake activity during seismic sequences can occur off the main activated structures and within large rock volumes. Ductile crustal deformation can cause off-fault and diffuse microseismicity, which obeys to different scaling laws than on fault seismicity. Lithological heterogeneities in the rock units composing the seismogenic layer[55] strongly influence seismicity distributions and seismicity rates. Our findings show that rheological behaviour of crustal rocks needs to be considered to explain the complexities of seismic sequences and advance our understanding of earthquake physics, including earthquake scaling laws.

Methods

The statistics of magnitude - frequency distribution (MFD) of earthquakes is usually modeled with an exponential function, called Gutenberg-Richter law, written as: , where N(M) represents the number of events with magnitude larger than M, *a* represents the productivity and *b* controls the relative rate of small and large earthquakes. Estimating the *b*-value appears trivial in theory but not in practice[33, 35].

Here we use the high-resolution catalog by[10] and we divide the catalog into on-fault and off-fault seismicity occurring within Triassic Evaporites (see Fig. 2 on the main text).

On-fault

For on-fault seismicity we selected all the events having a distance less than 0.5 km from the fault hosting the Norcia mainshock. The fault plane is defined with a strike of 155°, obtained from the mainshock moment tensor[16], and dip of 40°, inferred from aftershocks distribution, cf. for example Fig. 2b of the main text. We selected earthquakes at depth between 2km and 6.1 km (hypocentral depth)

where microseismicity distribution clearly shows the fault geometry, and for a distance along strike direction less than 5 km (Supplementary Fig. 2). Beyond this distance the activated fault plane is not clearly imaged by aftershocks distribution.

Off-fault

For off-fault seismicity we selected earthquakes occurring in:

a) the thick zone of diffuse seismicity located down-dip in the hangingwall of the mainshock rupture and nucleating within the Triassic Evaporites (cf. Fig. 2 of the main text). We will subsequently refer to this feature as, down-dip hangingwall seismicity, DHwS. These earthquakes have been selected within a volume with the dimensions 9.5 km orthogonal to the strike of the mainshock, 10 km along strike and 3 km along depth, from 6.104 km to 9.104 km, i.e., below the hypocentral depth (Supplementary Fig. 3);

b) kilometres long subvertical clusters of seismicity nucleating within Triassic Evaporites (cf. Fig. 2 of the main text). One of this cluster (blue in Supplementary Fig. 4) is well-defined defined in space, the other two (red and green in Supplementary Fig. 4) represent a series of sub-vertical clusters that we merged to achieve a reasonable number of earthquakes for the *b*-value analysis. Since the inputs for this space selection criterium are lon, lat and depth, a limited number of earthquakes belonging to these groups are not contained within the clusters.

Once defined the criteria to depict the geometry of on-fault vs. off-fault seismicity, we also adopted a selection in time. For on-fault and DHwS we selected two time-periods the first one collects the seismic activity before the occurrence of the Mw 5.9 Visso event on 26 October and the Mw 6.5 Norcia event on 30 October. The second period extends from 15 August 2016 to 15 August 2017, corresponding to the entire catalogue published in[10]. The selected time windows for the clusters are related to the occurrence of the events composing the clusters: cluster C1 occurred mainly on December 2016 while C2 and C3 have been recorded during the two months preceding the Norcia main event.

To calculate the *b-value* (Supplementary Table 1) we apply the following steps:

1) For any considered time-interval we excluded the short-term aftershock incompleteness (STAI) from the catalogs, adopting the same criteria of [35];

2) We derived the *b*-value with the Maximum Likehood Extimation (MLE) method according to the corrected formula[34] that accounts for the discrete nature of magnitude values. The adopted catalog has a magnitude discretization, or binning, of $\Delta M=0.01$.

3) We used the Lilliefors-based magnitude of completeness $M_c^{\text{Lilliefors}}$ [35] as minimum magnitude in the MLE formula to avoid severe bias in the *b*-value estimation. Through a recursive test adopted to check the null hypothesis, the $M_c^{\text{Lilliefors}}$ is defined as the lowest magnitude level above which the MFD can be considered an exponential function.

4) Number of events in each subset is large enough (>1500) to have stable *b*-values.

The inferred b-values for all the considered subsets and time interval are reported in Supplementary Table 1 together with the 95% confidence intervals and $M_c^{Lilliefors}$ values.

Widening the on-fault at 1 km or extending the DHwS of ± 1 km along strike yields essentially the same results.

Data availability: All data needed to evaluate the conclusions in the paper are present in the paper and/or the Supplementary Information. Additional data related to this paper may be requested from the authors.

Declarations

Acknowledgments: We thank L. Chiaraluce, C. Marone, G. Pozzi and M. Scuderi for fruitful discussions.

Author contributions: CC conceptualized the idea together with NDP. ET performed the analysis on *b*-values with conceptual inputs from CC. All authors contributed to the data analysis, discussion, and interpretation of results. CC wrote the manuscript with the help of NDP.

Competing interests: All other authors declare they have no competing interests.

Correspondence and requests for materials should be addressed to C.C.

References

1. Waldhauser, F. & Ellsworth, W. L. A Double-Difference Earthquake Location Algorithm: Method and Application to the Northern Hayward Fault, California. Bull. Seism. Soc. Am. **90**, 1353–1368 (2000).
2. Zhu, W. & Beroza, G. C. PhaseNet: a deep-neural-network-based seismic arrival-time picking method. Geophys. J. Int. **216**, 261–273 (2019).
3. Waldhauser, F., Ellsworth, W. L., Schaff, D. & Cole, A. Streaks, multiplets, and holes: High-resolution spatio-temporal behavior of Parkfield seismicity. Geophys. Res. Lett. **31**, L18608 (2004).
4. Ross Z. E. et al. Hierarchical interlocked orthogonal faulting in the 2019 Ridgecrest earthquake sequence. Science **366**, 346–351 (2019).
5. Shelly, D. R. A High-Resolution Seismic Catalog for the Initial 2019 Ridgecrest Earthquake Sequence: Foreshocks, Aftershocks, and Faulting Complexity. Seismol. Res. Lett. **91**, 1971–1978 (2020).

6. Valoroso, L., Chiaraluce, L., Piccinini, D., Di Stefano, R., Schaff, D. &Waldhauser, F. Radiography of a normal fault system by 64,000 high-precision earthquake locations: The 2009 L'Aquila (central Italy) case study. J. Geophys. Res. Solid Earth *118*, doi:10.1002/jgrb.50130 (2013).
7. Ross, Z. E., Hauksson, E. & Ben-Zion, Y. Abundant off-fault seismicity and orthogonal structures in the San Jacinto fault zone. Sci. Adv. **3**: e1601946 (2017)
8. Cheng, Y. & Ben-Zion, Y. Variations of earthquake properties before, during, and after the 2019 M7.1 Ridgecrest, CA, earthquake. Geophysical Research Letters **47**, e2020GL089650 (2019).
9. Kwiatek, G., et al. Controlling fluid-induced seismicity during a 6.1-km-deep geothermal stimulation in Finland. Sci. Adv. **5**, eaav7224 (2019).
10. Tan, Y. J., Waldhauser, F., Ellsworth, W. L., Zhang, M., Zhu, W., Michele, M., Chiaraluce, L., Beroza, G. C. & Segou, M. Machine-Learning-Based High-Resolution Earthquake Catalog Reveals How Complex Fault Structures Were Activated during the 2016–2017 Central Italy Sequence. The Seismic Record **1**, 11–19 (2021).
11. Shelly, D.R., Ellsworth, W. L., & Hill D.P.. Fluid-faulting evolution in high definition: Connecting fault structure and frequency-magnitude variations during the 2014 Long Valley Caldera, California, earthquake swarm. J. Geophys. Res. Solid Earth **121**, 1776–1795 (2016).
12. Valoroso, L., Chiaraluce, L. & Collettini, C. Earthquakes and fault zone structure. *Geology* <bi>42</bi>, *343–346* (2014).
13. Savage, H. M., Keranen, K. M., Schaff, D. P. & Dieck, C. Possible precursory signals in damage zone foreshocks. Geophys. Res. Lett. **44**, 5411–5417 (2017).
14. Barchi, M. R., Carboni, G., Michele, M., Ercoli, M., Giorgetti, C., Porreca, M., Azzaro, S. & Chiaraluce, L. The influence of subsurface geology on the distribution of earthquakes during the 2016-–2017 Central Italy seismic sequence. Tectonophysics **807**, 228797 (2021).
15. Villani, F., Civico, R., Pucci S., et al. A database of the coseismic effects following the 30 October 2016 Norcia earthquake in Central Italy. Sci Data **5**, 180049 (2018).
16. Scognamiglio, L., Tinti, E., Casarotti, E., Pucci, S., Villani, F., M. Cocco et al. Complex fault geometry and rupture dynamics of the MW 6.5, 30 October 2016, central Italy earthquake. Journal of Geophysical Research **123**, 2943–2964 (2018).
17. Ercoli, M., Forte, E., Porreca, M., Carbonell, R., Pauselli, C., Minelli, G. & Barchi, M. R. Using seismic attributes in seismotectonic research: an application to the Norcia M_W = 6.5 earthquake (30 October 2016) in central Italy. Solid Earth **11**, 329–348 (2020).
18. Chiaraluce L. et al. The 2016 Central Italy Seismic Sequence: A First Look at the Mainshocks, Aftershocks, and Source Models. Seism. Res. Lett. **88**, 757–771 (2017).
19. Improta, L. et al. Multi-segment rupture of the 2016 Amatrice-Visso-Norcia seismic sequence (central Italy) constrained by the first high-quality catalog of early Aftershocks. Scientific Reports **9**, 6921 (2019).

20. Michele, M., Chiaraluce, L., Di Stefano, R. & Waldhauser, F. Fine-scale structure of the 2016–2017 Central Italy seismic sequence from data recorded at the Italian National Network. *Journal of Geophysical Research: Solid Earth* **125**, e2019JB018440 (2020).
21. Waldhauser, F., Michele, M., Chiaraluce, L., Di Stefano, R. & Schaff, D. P. Fault planes, fault zone structure and detachment fragmentation resolved with high- precision aftershock locations of the 2016–2017 central Italy sequence. *Geophysical Research Letters* **48**, e2021GL092918 (2021).
22. Bally, A. W., Burbi, L., Cooper, C. & Ghelardoni, R. Balanced cross-sections and seismic reflection profiles across the central Apennines. Mem. Soc. Geol. Ital. **35**, 257–310 (1986).
23. Barchi, M. R., Minelli, G. & Pialli, G. The crop 03 profile: a synthesis of results on deep structures of the Northern Apennines. Mem. Soc. Geol. Ital. **52**, 383–400 (1998).
24. Miller, S. A., Collettini, C., Chiaraluce, L., Cocco, M, Barchi, M. R. & Kaus, B. Aftershocks driven by a high pressure CO_2 source at depth. Nature **427**, 724–727 (2004).
25. Mirabella, F., Barchi, M. R., Lupattelli, A., Stucchi, E. & Ciaccio, M.G. Insights on the seismogenic layer thickness from the upper crust structure of the Umbria–Marche Apennines (Central Italy). Tectonics **27**, TC1010 (2008).
26. Porreca, M., Minelli, G., Ercoli, M., Brobia, A., Mancinelli, P., Cruciani, F., Giorgetti, C. Carboni, C., Mirabella, F., Cavinato, G., Cannata, A., Pauselli, C. & Barchi, M. R. Seismic reflection profiles and subsurface geology of the area interested by the 2016–2017 earthquake sequence (Central Italy). Tectonics **37**, 1–22 (2018).
27. Buttinelli M. et al., The impact of structural complexity, fault segmentation, and reactivation on seismotectonics: Constraints from the upper crust of the 2016–2017 Central Italy seismic sequence area. Tectonophysics **810**, 228861 (2021).
28. Kanamori, H. & Brodsky, E. E. The Physics of Earthquakes. Rep. Prog. Phys. **67**, (2004).
29. Schorlemmer, D., Wiemer, S. & Wyss, M. Variations in earthquake-size distribution across different stress regimes. Nature **437**, 539–542 (2005).
30. C. H., Scholz, The frequency-magnitude relation of microfracturing in rock and its relation to earthquakes. Bulletin of the Seismological Society of America 58, 399–415 (1968).
31. Goebel, T. H., Kwiatek, G., Becker, T. W., Brodsky, E. E. & Dresen, G. What allows seismic events to grow big?: Insights from b-value and fault roughness analysis in laboratory stick-slip experiments. Geology 45, 815–818 (2017).
32. Gulia, L. & Wiemer, S. Real-time discrimination of earthquake foreshocks and aftershocks. Nature **574**, 193–199 (2019).
33. Cousineau, K., Lay, T. & Brodsky, E. E. Two Foreshock Sequences Post Gulia and Wiemer (2019). Seismol. Res. Lett. 91, 2843–2850 (2020).
34. Utsu, T. A Statistical Significance Test of the Difference in b-value between Two Earthquake Groups. Journal of Physics of the Earth **2**, 37–40 (1966).

35. Herrmann, M. & Marzocchi, W. Inconsistencies and Lurking Pitfalls in the Magnitude– Frequency Distribution of High-Resolution Earthquake Catalogs. Seismol. Res. Lett. **20**,1–14 (2021).
36. Davis, D. M. & Engelder, T. The role of salt in fold-and-thrust belts. Tectonophysics **119**, 67–88 (1985).
37. Stiros, S. Geodetic evidence for mobilization of evaporites during the 1997 Strophades (W Hellenic Arc) Mw 6.5 earthquake. J. Geophys. Eng. **2**, 111–117 (2005).
38. Nissen, E., Jackson, J., Jahani, S. & Tatar, M. Zagros "phantom earthquakes" reassessed—The interplay of seismicity and deep salt flow in the Simply Folded Belt? J. Geophys. Res. Solid Earth **119**, (2014).
39. Trippetta, F., Collettini, C., Barchi, M. R., Lupattelli, A. & Mirabella, F. A multidisciplinary study of a natural example of a CO2 geological reservoir in central Italy. International Journal of Greenhouse Gas Control **12**, 72–83 (2013).
40. De Paola, N., Collettini, C., Faulkner, D. R. & Trippetta, F. Fault zone architecture and deformation processes within evaporitic rocks in the upper crust, Tectonics **27**, (2008)
41. Sibson, R. H. Fault rocks and fault mechanisms, J. Geol. Soc. Lond. **133**, 191–213 (1977).
42. Rutter, H. E. On the nomenclature of mode of failure transitions in rocks, Tectonophysics **122**, 381–387 (1986).
43. Handin, J. & Fairbairn, H. W. Experimental deformation of Hasmark dolomite. Bull. Geol. Soc. Am. **66**, 1257–1274 (1956).
44. De Paola, N., Faulkner, D. R. & Collettini, C. Brittle versus ductile deformation as the main control on the transport properties of low-porosity anhydrite rocks. J. Geophys. Res. **114**, B06211, (2009).
45. Scuderi, M. M., Niemeijer, A., Collettini, C. & Marone C. Frictional Properties and Slip Stability of Active Faults within Carbonate-Evaporite Sequences: the Role of Dolomite and Anhydrite. EPSL **369**, 220–232 (2013).
46. Scuderi, M. M., Tinti, E., Cocco, M. & Collettini, C. The Role of Shear Fabric in Controlling Breakdown Processes During Laboratory Slow-Slip Events. J. Geophys. Res. Solid Earth **125**, (2020).
47. Volpe, G., Pozzi, G., Carminati E. et al. Frictional controls on the seismogenic zone: Insights from the Apenninic basement, Central Italy. *EPSL* **583**, (2022).
48. Carpenter, B. M., Scuderi, M. M., Collettini, C. & Marone, C. Frictional heterogeneities on carbonate-bearing normal faults: Insights from the Monte Maggio Fault, Italy. Journal of Geophysical Research **119**, (2014).
49. De Murtas, M., Fondriest, M., Balsamo, F., Clemenzi, L., Storti, F., Bistacchi, A. & Di Toro, G. Structure of a normal seismogenic fault zone in carbonates: The Vado di Corno fault, Campo Imperatore, central Apennines (Italy). J. Struct. Geol. **90**, 185–206 (2016).
50. Smeraglia, L., Bettucci, A., Billi, A., Carminati, E., Cavallo, A., Di Toro, G., Natali, M., Passeri, D., Rossi, M. & Spagnuolo, E. Microstructural evidence for seismic and aseismic slips along clay-bearing, carbonate faults. J. Geophys. Res. Solid Earth **122**, (2017).

51. Passelègue, F. X., Aubry, J., Nicolas, A., Fondriest, M., Deldicque, D., Schubnel, A. & Di Toro, G. From fault creep to slow and fast earthquakes in carbonates. Geology **44**, 607–610 (2019).
52. Chiarabba, C., De Gori, P., Cattaneo, M., Spallarossa, D. & Segou, M. Faults geometry and the role of fluids in the 2016–2017 Central Italy seismic sequence. Geophysical Research Letters **45**, 6963–6971.
53. Schaff, D. P., Bokelmann, G. H. R. & Beroza, G. C. High-resolution image of Calaveras Fault seismicity. J. Geophys. Res. Solid Earth **107**, (2002).
54. Scholz, C. H. The mechanics of earthquakes and faulting. *Cambridge University Press*, (2019).
55. Barnes P. M. et al. Slow slip source characterized by lithological and geometric heterogeneity. Sci. Adv. **6**, eaay3314 (2020).

Figures

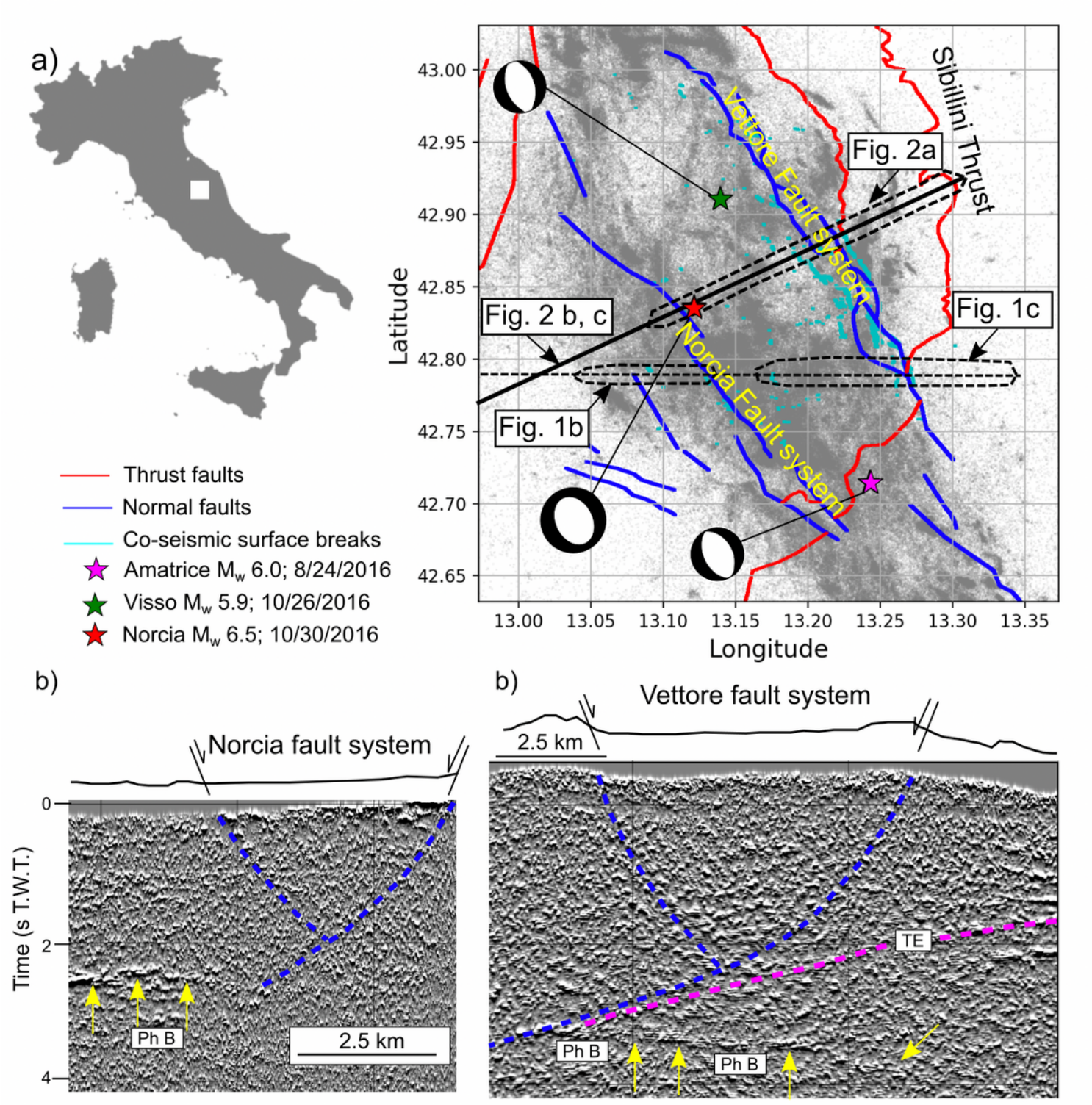

Figure 1

Map of the sequence with surface and subsurface geology. (a), Map view of the study area, gray dots represent located earthquakes from Amatrice to 40 days after Norcia[10]. Co-seismic surface breaks along the Vettore and Norcia fault systems from[15], and moment tensor solutions[16]. **(b)** and **(c),** seismic images of the subsurface geology (seismic traces are reported in a). Blue dashed lines are the Norcia and Vettore

fault systems at depth. TE is the reflector corresponding to the top of Triassic Evaporites, Ph B are the reflectors of the phyllitic basement (details in [14, 17]).

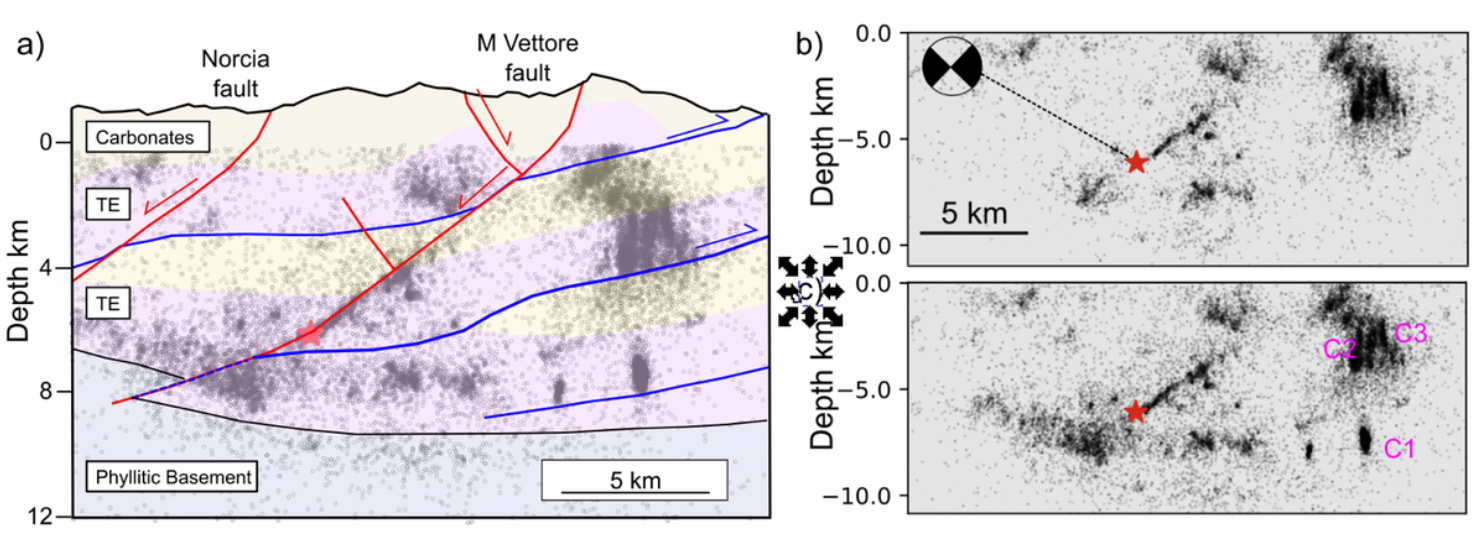

Figure 2

Seismicity vs. geology. (a), Cross section (trace in Fig. 1) integrating surface and subsurface geology (details in[14]) with the earthquake distribution. **(b)** and **(b),** details of seismicity distributions: in (b) seismicity from Amatrice (8/24/2016) to Norcia (10/30/2016) and (b) from Amatrice up to 40 days after Norcia. Cross-section perpendicular to the strike (155°, from the moment tensor solution[16]) of the mainshock (red star) with all events within 1 km from the cross-section. Many microearthquakes occurs within large rock volumes of Triassic Evaporites, TE. This off-fault seismicity mainly occurs in: i) a 6-8 km wide and up to 4 km thick zone of diffuse seismicity, located down-dip in the hangingwall of the Norcia seismic rupture and is mainly illuminated after the Norcia mainshock (cf. b vs. c); ii) sub-vertical clusters of seismicity that are present at different crustal levels (C1-C3).

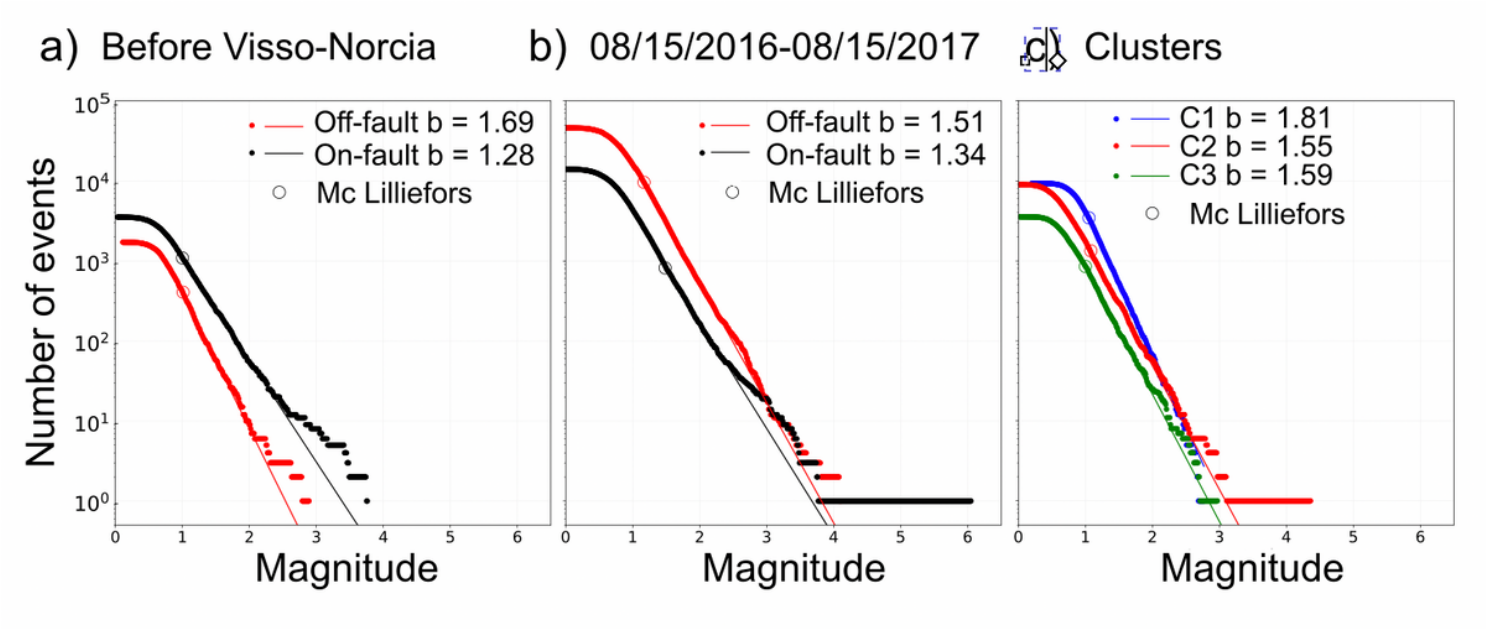

Figure 3

On-fault vs. off-fault frequency-magnitude distributions. (a), before the two major events of Visso and Norcia. **(b),** In the year after the beginning of the sequence. **(c)**, in clusters occurring within Triassic Evaporites (see location in Fig. 2c). Details of the selection of the on-fault vs. off faults datasets are reported in Methods and Supplementary Fig. 2-4.

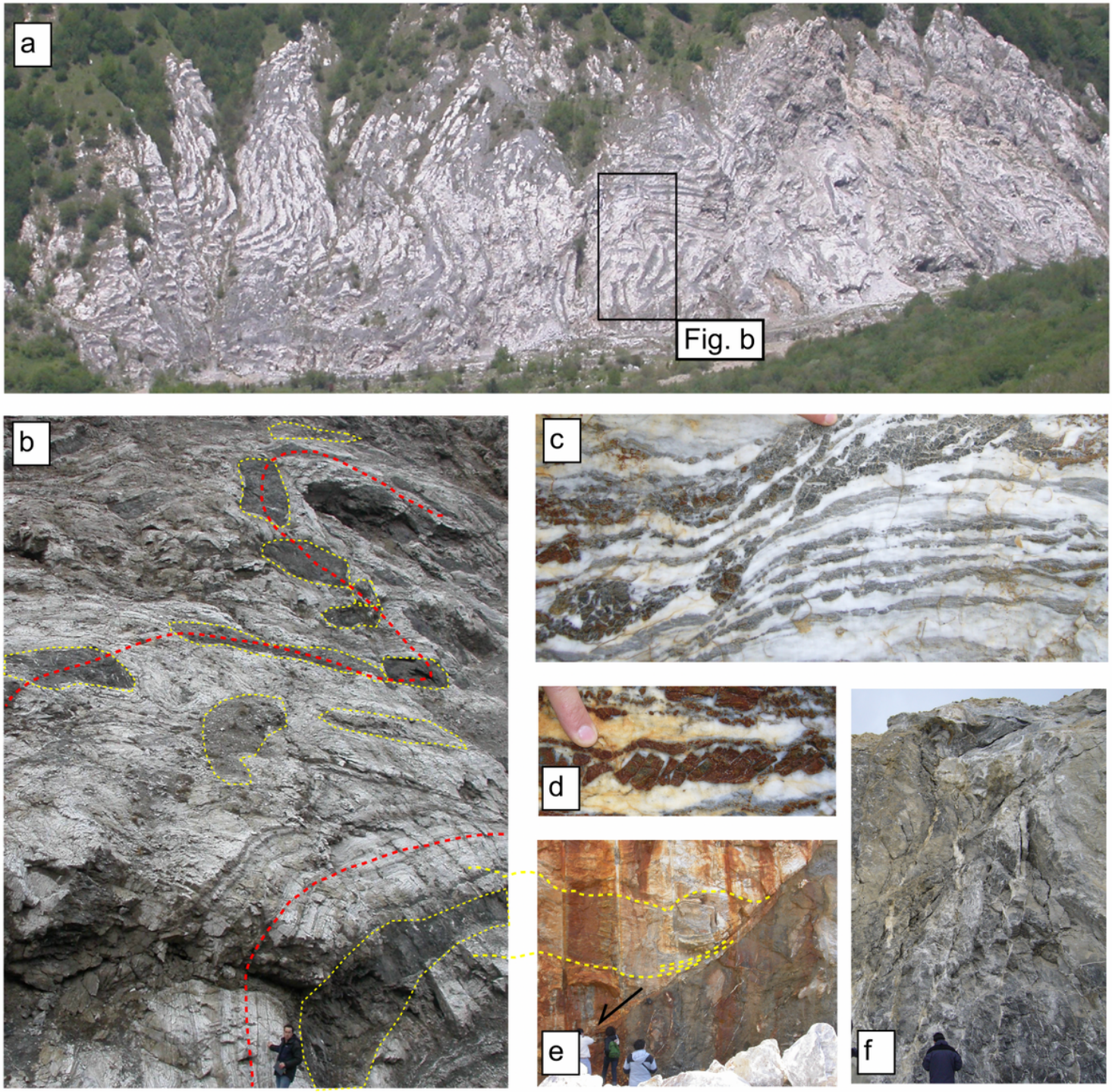

Figure 4

Bimodal style of deformation of Triassic Evaporites. **(a)** and **(b),** foliated and folded gypsum/anhydrite rocks (white) with boudinaged dolostone (grey lenses highlighted by dashed yellow lines). The dashed red line marks the geometry of the fold. **(c),** gneissic transposed fabric affected by normal faulting and boudinage of the dolostone layers. **(d),** Domino-like structure with brittle faulting on dolostones and ductile deformation on gypsum/anhydrite. **(e),** Small-displacement (meters), gently dipping normal fault at the boundary between gypsum/anhydrite rocks in the hangingwall (dashed yellow lines mark the

foliation) and fractured dolostone in the footwall. **(f),** Intense subvertical hydrofracturing within the dolostones.

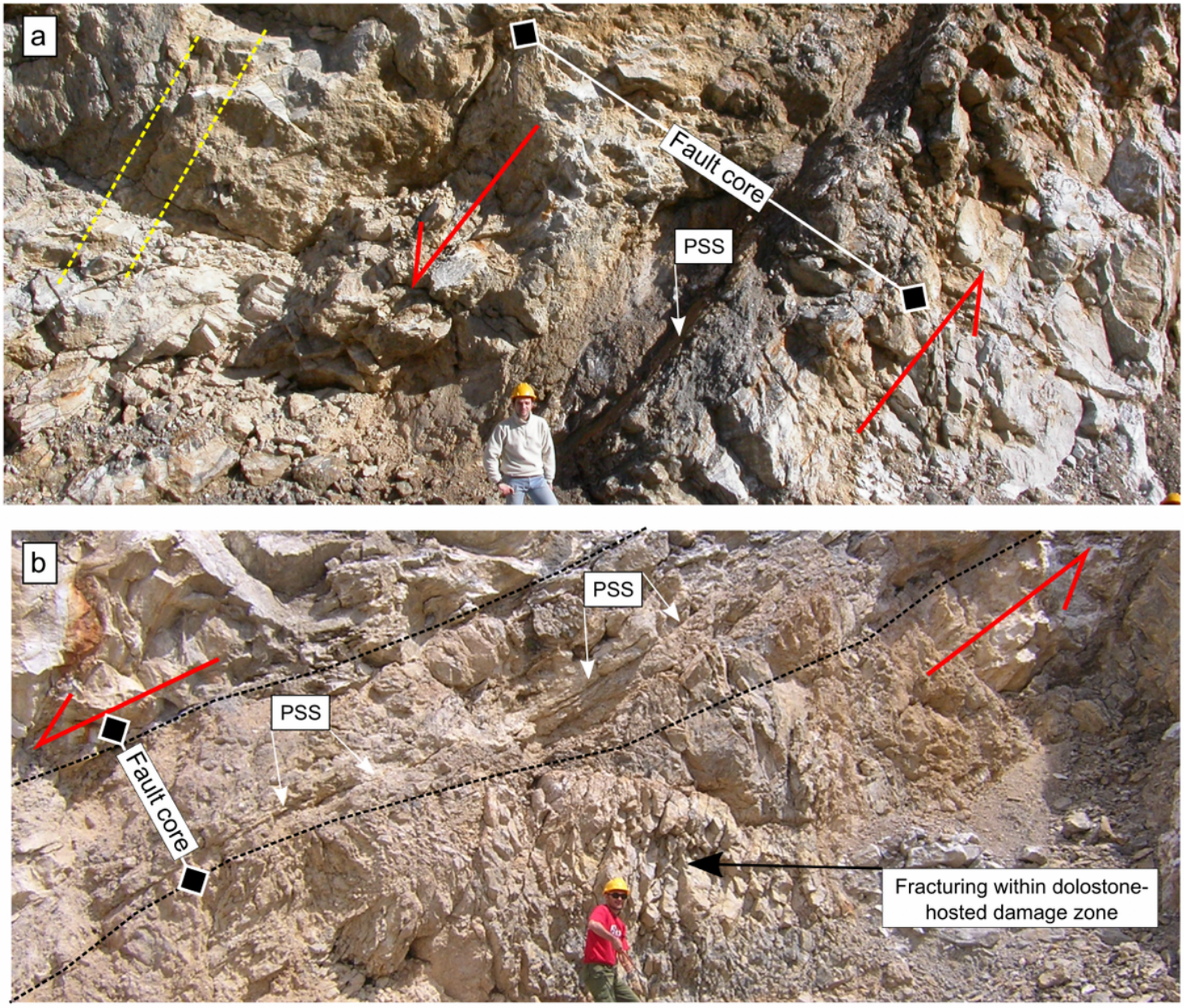

Figure 5

Brittle faulting along major normal faults within TE. (a) and **(b),** Large displacement (hundreds of meters) normal faults with brittle deformation, characterized by grain-size reduction and localization along principal slipping surfaces, PSS. The dashed yellow line marks the fault parallel foliation within the gypsum-anhydrites rocks.

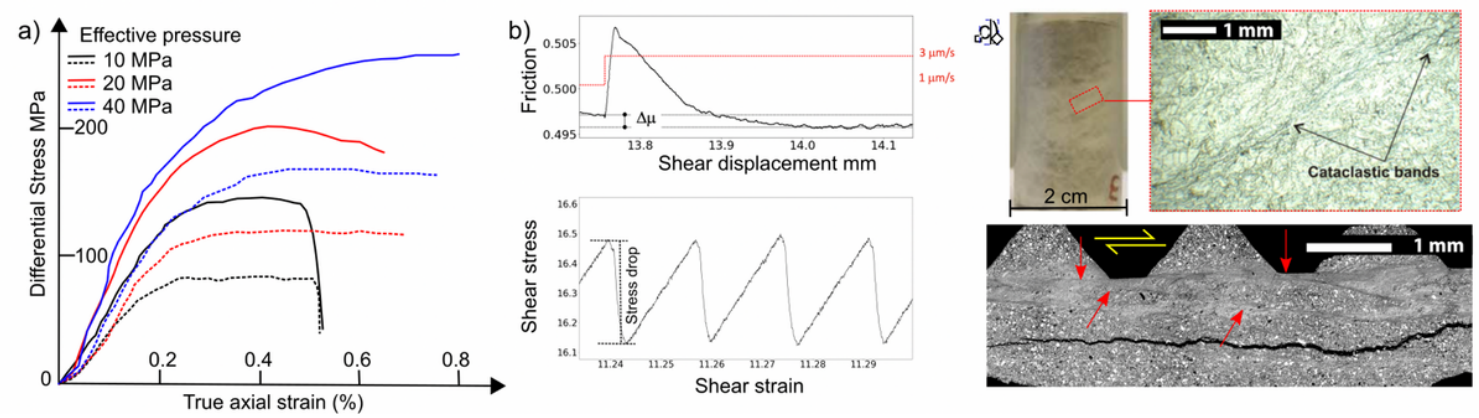

Figure 6

Rock vs. fault rheology. (a), Summary of triaxial tests on anhydrites cylindrical samples (details [44]). Experiments were conducted at constant confining pressure, P_c = 100 MPa, and fluid pressure, P_f, of 60, 80 and 90 MPa, with a resulting effective pressure, Pe = P_c -P_f, 40, 20 and 10 MPa. Dashed and solid lines for axial loading parallel and orthogonal to the foliation respectively. Anhydrite deformation is ductile and turns into brittle for high values of fluid pressure. **(b),** Frictional rheology of anhydrite-dolomite fault gouge (details in [46]): (top panel) reduction in friction, Dm, following a velocity step (from 1 to 3 mm/s) resulting in a velocity weakening behaviour; stick-slip cycles (bottom panel) with stress drop of about 0.35 MPa. **(c),** Ductile deformation of anhydrite rocks during triaxial tests produces distributed cataclastic bands (top panel) whereas stick-slip instabilities on anhydrite-dolomite fault gouges are favored by slip localization (bottom panel).

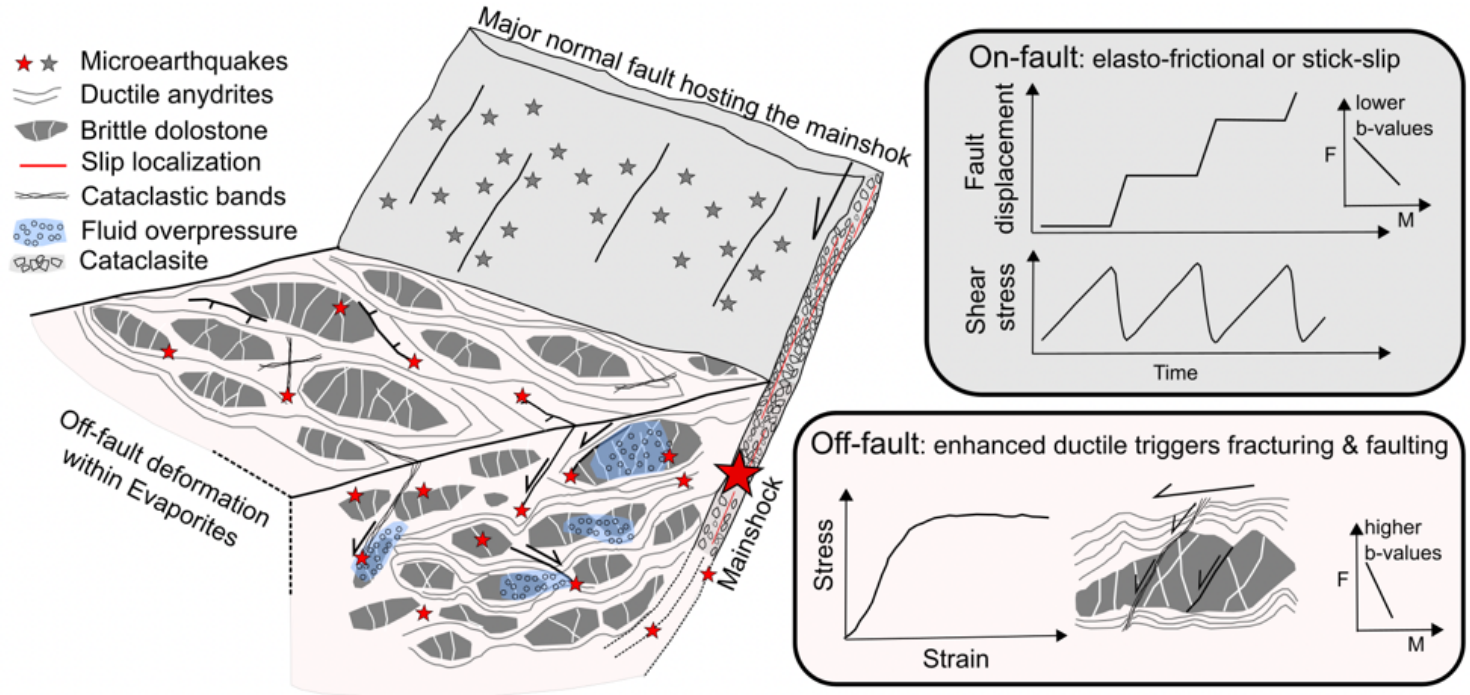

Figure 7

The role of rheology for on-fault vs. off-fault seismicity. Cataclasis and slip localization along major normal faults produce fault rocks with frictional properties that promote earthquake nucleation via their stick-slip behaviour. During the seismic sequence enhanced ductile deformation of the anhydrites favours distributed fracturing and faulting of dolostones, brittle failure of anhydrites and reactivation of small displacement faults. Distributed deformation on large rock volumes of TE is associated to higher *b*-values of the earthquake frequency(F)-magnitude(M) distribution whereas on-fault seismicity shows lower *b*-values.

Supplementary Files

This is a list of supplementary files associated with this preprint. Click to download.

- SuppInfo.docx